Applied Catalysis B: Environment and Energy 394 (2026) 126821

Contents lists available at ScienceDirect

Applied Catalysis B: Environment and Energy

journal homepage: www.elsevier.com/locate/apcatb

Lewis acid-mediating local alkaline microenvironment for efficient oxygen evolution

Fengli Wei [a], Jinghao Shen [a], Zuyang Luo [a], Panpan Sun [b], Heyang Liu [a], Xiaofeng Shi [c], Bo Liu [d], Xiulin Yang [a,*], Dapeng Cao [b], Zhenbo Wang [d], Yongfa Zhu [e,*], Bin Wu [f,*]

[a] Guangxi Key Laboratory of Low Carbon Energy Materials, School of Chemistry and Pharmaceutical Sciences, Guangxi Normal University, Guilin, Guangxi 541004, China
[b] State Key Laboratory of Organic-Inorganic Composites, Beijing University of Chemical Technology, Beijing 100029, China
[c] School of Environment and Safety Engineering, North University of China, Taiyuan 030051, China
[d] State Key Laboratory of Space Power-Sources, MIIT Key Laboratory of Critical Materials Technology for New Energy Conversion and Storage, School of Chemistry and Chemical Engineering, Harbin Institute of Technology, Harbin, Heilongjiang 150001, China
[e] Department of Chemistry, Tsinghua University, Beijing 100084, China
[f] School of Materials Science and Engineering, Nanyang Technological University, 50 Nanyang Avenue, Singapore 639798, Singapore

ARTICLE INFO

Keywords:
Hard-soft acid-base principle
Local alkalinity
Hydrogen bonding interactions
Oxygen evolution reaction
AEM water electrolyzer

ABSTRACT

Regulating the coordination environment of catalytic active sites is critical for improving the oxygen evolution reaction (OER) in alkaline media. In this work, a rational strategy based on hard-soft-acids-base principle is proposed to finely control the local environment around active sites by introducing hard Lewis-acid (W^{6+}) sites. In situ characterizations indicate that the Lewis acid selectively captures hydroxide ions (which act as hard Lewis bases), thereby modifying the hydrogen-bonding network and establishing a stable, hydroxide-enriched layer near the active regions. This persistently alkaline interface inherently inhibits chemical degradation, particularly under high-current conditions. Computational studies verify that the hydroxyl capture promotes and secures the *OOH transition states on the catalyst surface, reducing the energy barrier of the rate-limiting step. The designed Ni_3Se_2 catalyst, incorporating Lewis acidic W^{6+} centers ($Ni_3Se_2/NiWO_4$), demonstrates outstanding catalytic activity in alkaline electrolyte, requiring only 235 mV overpotential to reach 10 mA cm^{-2} and maintaining stable operation for over 500 h at 100 mA cm^{-2}. When incorporated within an anion exchange membrane water electrolyzer (AEMWE), the $Ni_3Se_2/NiWO_4$-based cell exhibits exceptional endurance, operating continuously for 96 h at an industrial-level current density of 1 A cm^{-2}. This study highlights Lewis acid-mediated active-site regulation as an effective strategy to control OER intermediates and enhance catalytic performance in alkaline water electrolysis.

1. Introduction

Hydrogen is a clean energy carrier with a high gravimetric energy density (142 kJ g^{-1}) [1]. Anion exchange membrane water electrolysis (AEMWE) for green hydrogen production using renewable electricity from wind and solar power is an intriguing possibility to alleviate the current global energy and environmental crisis [2–6]. However, the successive four-electron transfer process conversion involved in the anodic oxygen evolution reaction (OER) leads to its inherent slow dynamics, which greatly impedes the efficiency of hydrogen production from electrolyzed water [7–11]. Electrocatalytic water-splitting is a triphasic process involving a solid electrodes, electrolytes, and gas products [12–15]. A typical pathway of OER reaction includes three steps: charge transfer and surface transformations (such as reactants chemisorb and products desorb from the electrode surface), charge transport, and mass transfer. Significant efforts are being focused on the surface regulation step by increasing the density of OER active sites and regulating the binding energies to balance the adsorption/desorption of intermediates [16–20].

According to the prevailing mechanism for alkaline OER, one hydroxide (OH^-) is first adsorbed onto the metal surface to form M−OH bond (where M denotes metals), which is deprotonated to create M−O, and further experiences hydroxylation to produce M−OOH. Finally, the M−OOH reacts with OH^-, leading to the formation of H_2O and adsorbed

* Corresponding authors.
E-mail addresses: xlyang@gxnu.edu.cn (X. Yang), zhuyf@tsinghua.edu.cn (Y. Zhu), bin.wu@ntu.edu.sg (B. Wu).

https://doi.org/10.1016/j.apcatb.2026.126821
Received 2 February 2026; Received in revised form 9 April 2026; Accepted 16 April 2026
Available online 17 April 2026
0926-3373/© 2026 Elsevier B.V. All rights are reserved, including those for text and data mining, AI training, and similar technologies.

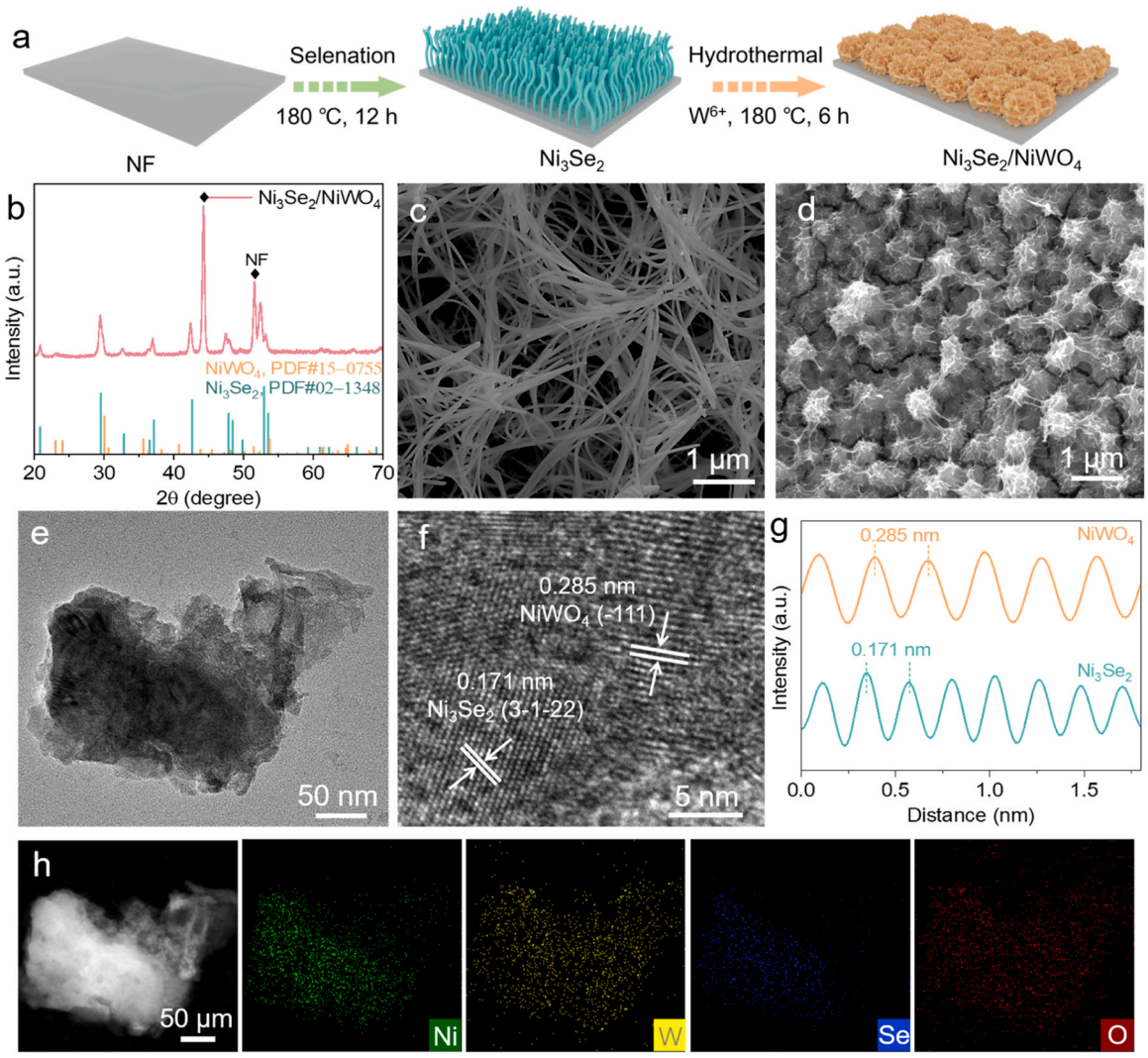

Fig. 1. Synthesis process and microscopy characterization. (a) Schematic diagram for the fabrication and (b) XRD pattern of $Ni_3Se_2/NiWO_4$. SEM images of (c) Ni_3Se_2 and (d) $Ni_3Se_2/NiWO_4$. (e) TEM image, (f) HR-TEM image, and (g) corresponding lattice spacing profiles of $Ni_3Se_2/NiWO_4$. (h) The HAADF-STEM and corresponding EDS mapping images of Ni, W, Se, and O elements in $Ni_3Se_2/NiWO_4$.

O_2 [21]. The binding ability of intermediates and charge transfer are always considered as the key parameters for determining the OER kinetics. The mechanism together with previous experimental studies [22,23], suggest that OER activity is directly related to the OH^- adsorption at the active sites. The OH^- adsorption is crucial for enhancing the OER performance since a higher number of OH^- adsorption processes on exposed active sites provide favorable conditions for subsequent kinetic steps. In the conventional alkaline OER, most OH^- anions are usually hydrated and their relatively low adsorption capabilities result in the major distribution on the outer Helmholtz plane (OHP), rather than the inner Helmholtz plane (IHP) where the reaction proceeds [24]. Following a Grotthuss-like mechanism, OH^- can exploit the hydrogen-bond network at the interface as a transport channel, where re-organization of interfacial water and hydrogen bonds facilitates their migration toward active sites [25]. A well-structured interfacial water network can effectively guide and pre-organize hydrated OH^- ions through hydrogen-bond interactions with their hydration shells, driving the OH^- to approach the IHP toward the downstream reactions, thus improving catalytic efficiency in alkaline electrolytes. Meanwhile, the quick depletion of OH^- ions would result in localized pH fluctuations (localized neutral or acidic micro-environments around the catalytic site), which degrade the catalyst's performance and longevity, especially during high current density operations [26]. So far, numerous efforts have been dedicated to facilitating desirable proton-electron diffusion and adsorption. Recent study by Dong' group show that intercalated squaric acid anions stabilizes OH^- through multiple hydrogen bond interactions, thus maintaining high catalytic interface alkalinity [27]. Strong electric field effect at nanotips [12] and the leaching of surface atoms [28] can also accelerate the conveyance of OH^-. In addition, it is reported that Lewis acid layers on the catalyst surface also can promote the OH^- adsorption. Ling et al. designed to coat a hard Lewis acid, Cr_2O_3, onto CoO_x catalyst to adjust alkalized microenvironment, thus achieving efficiently direct seawater electrolysis [29]. Lewis acid not only acts as an electron receptor to regulate the electron-rich state of the metal sites but also enhances local alkalinity to resist the rapid depletion of OH^- [30,31]. In particular, the W^{6+} doping sites with empty $5d^0$ characteristic are reported to efficiently adsorb H_2O and OH^- groups, facilitating the O−O coupling, thereby reducing the OER overpotential [32,33]. Consequently, finely tuning the microenvironment through modifing Lewis acid sites at the catalyst-electrolyte interface represents a potentially effective approach to enhance the activity and stability [34–36].

Herein, following the classic hard and soft acid base theory, we introduce a hard Lewis acid layer, tungstate (W sites) over the Ni_3Se_2 catalyst to capture hydroxyl anions (a hard Lewis base) and modulate hydrogen-bond network, thus tailoring localized alkalized

microenvironment. The existence of such *in-situ* generated local alkalinity creates a high-speed pathway for OH^- transport into active site and optimizes the adsorption of reaction intermediates, thus achieving efficient OER. Specifically, experimental and theoretical studies verify that the introduction of Lewis acid sites can regulate the interfacial hydrogen bonding interactions, avidly capturing significant volumes of OH^- groups at the reactive sites, which plays a critical role in prolonging the catalytic lifespan. As a result, the hierarchical $Ni_3Se_2/NiWO_4$ exhibit a low overpotential of 235 mV at 10 mA cm^{-2} and maintaining stable operation at 100 mA cm^{-2} for 500 h, surpassing even the most recently reported non-precious metal-based catalysts. Furthermore, The $Ni_3Se_2/NiWO_4$-based electrode exhibits remarkable durability in an anion exchange membrane water electrolyzer (AEMWE), achieving stable operation for ~100 h at 1 A cm^{-2}, which meets a key industrial performance benchmark. The proposed microenvironment modulation strategy provides a fundamental insight for designing advanced AEMWE catalysts, enabling simultaneously superior activity and operational stability via precise local environment control.

2. Experimental section

2.1. Chemicals and reagents

Tungsten hexachloride (WCl_6, 98.0%), potassium hydroxide (KOH, 90.0%), sodium borohydride ($NaBH_4$, 98%), selenium (Se, 99.9%), ethanol (C_2H_5OH, 99.7%), hydrochloric acid (HCl, 37.0%). Ni foam (NF) was purchased from commercial company. The 5 wt% Nafion solution and commercial Pt/C (20 wt% for platinum) were all purchased from Adamas Chemical Reagent Co. Ltd. RuO_2 powder was synthesized by directly annealing $RuCl_3{\cdot}3\ H_2O$ (37%, Inno-chem) at 400 °C in air. The deionized water (18.2 MΩ cm) was produced by an ultrapure water system (Millipore). All reagents and chemicals were commercially available and without further purification.

2.2. Preparation of Ni_3Se_2

A piece of NF (1 ×3 cm^2) was sequentially washed with HCl, ethanol, and deionized water to ensure thorough cleaning before use. For the preparation of NaHSe solution, 0.059 g Se powder was added into 1.5 mL deionized water containing 0.065 g $NaBH_4$. After gentle stirring for several minutes, a clear NaHSe solution was obtained. The freshly prepared NaHSe solution was added into 30 mL ethanol. Then the solution was transferred into 50 mL Teflon-lined stainless steel autoclave, along with a pretreated NF substrate, and maintained at 180 ℃ for 12 h in an electric oven. Upon gradual cooling to room temperature, the sample was collected and washed with water and ethanol several times and then dried at 60 ℃.

2.3. Preparation of $Ni_3Se_2/NiWO_4$

0.4 mmol WCl_6 was dissolved in 30 mL ethanol, and stirred for 1 h to form light blue solution. Next, the mixture solution and pretreated Ni_3Se_2 were together transferred into 50 mL Teflon-lined stainless steel autoclave and heated at 180 ℃ for 6 h. After naturally cooled down to room temperature, the production was collected, rinsed multiple times with water and ethanol, and then dried at 60 °C. A series of $Ni_3Se_2/NiWO_4$ samples were prepared by adjusting the WCl_6 dosage to 0.35 mmol, 0.40 mmol, and 0.45 mmol, respectively, while maintaining other hydrothermal conditions (180 °C, 6 h) unchanged.

2.4. Preparation of RuO_2 and 20 wt% Pt/C

The commercial $RuCl_3{\cdot}3\ H_2O$ was directly calcined at 400 °C for 3 h in the air to obtain RuO_2 powder. And then 2 mg RuO_2 or 20 wt% commercial Pt/C was dispersed into a mixture of 50 μL deionized water, 250 μL ethanol and 5 μL 5 wt% Nafion, respectively. The mixture was ultrasonically treated for at least 30 min to form a uniform catalyst ink, then dropped onto the surface of NF (1 cm × 1 cm) and dried naturally in the air.

3. Results and discussion

As illustrated in Fig. 1a, a self-supporting $Ni_3Se_2/NiWO_4$ heterostructure was constructed by a two-step procedure. Based on the classic hard and soft acid−base theory, [31] where hard acids preferentially bind with hard bases, we prsopose the introduction of hard Lewis acid species on the host-catalyst to capture hydroxy (a hard Lewis base) and further regulate the interfacial microenvironment of active Ni sites. To validate this hypothesis, we attempted to modify tungstate (W sites), which can act as hard Lewis acids, onto the Ni_3Se_2 catalyst, resulting interfacial characteristics. The commercial nickel foam (NF) with a porous structure and goodchemical/mechanical stability is selected as both substrate and Ni source for Ni_3Se_2 growth. Initially, NF was selenidized to form the high crystalline Ni_3Se_2, and then $NiWO_4$ nanowalls were grown on the 3D Ni_3Se_2 by a hydrothermal process to deliver the final heterostructure. This method features the epitaxial growth of $NiWO_4$ on Ni_3Se_2 nanowires, providing a structural basis for strong interfacial geometric and electronic interaction between $NiWO_4$ and Ni_3Se_2. The crystallographic texture of the obtained catalysts was firstly elucidated by X-ray diffraction (XRD) patterns. The direct *in-situ* hydrothermal growth of nickel selenide nanowires on NF as the precursor was indexed to be trigonal Ni_3Se_2 (PDF#02–1348), as shown in Figure S1. The monoclinic tungstate ($NiWO_4$, PDF#15–0755) assembles with Ni_3Se_2 to constitute the $Ni_3Se_2/NiWO_4$ composite (Fig. 1b). Moreover, the XRD Rietveld refinement method is applied to verify the crystal structure of Ni_3Se_2 and $NiWO_4$ in Figure S2. The fitting parameters in Table S1 and calculated patterns indicate acceptable correlation between observed and calculated XRD patterns. To visualize the morphologies and microstructures of the as-prepared materials, the images from scanning electron microscopy (SEM) experiment were collected. Figure S3a and S3b shows the low-magnification SEM image for NF after selenization, indicating its surface is fully covered by densely packed Ni_3Se_2 film. The magnified imagery in Fig. 1c demonstrates the formation of interconnected Ni_3Se_2 nanowires, usually 40–80 nm in diameter and up to several micrometers in length. The nanorod arrays on a self-sustaining electrode framework offer an expansive surface conducive to accelerated mass transport, particularly at heightened current densities. The morphology of $Ni_3Se_2/NiWO_4$ are subsequently depicted in Figure S3c and Fig. 1d, where uniform nanosheets are densely and vertically grown on the Ni_3Se_2 substrate, forming interconnected network of nanowalls. The morphology evolution from Ni_3Se_2 nanowires to $Ni_3Se_2/NiWO_4$ nanowalls is driven by seed-induced heterogeneous nucleation and directional self-assembly of $NiWO_4$ nanosheets, which is governed by interfacial energy minimization. [37] Such intricate configuration facilitates enhanced structural stability and efficient mass transport. [38,39] Transmission Electron Microscopy (TEM) reiterates morphology of $Ni_3Se_2/NiWO_4$ (Fig. 1e). The high-resolution TEM (HR-TEM) image of $Ni_3Se_2/NiWO_4$ manifests clear lattice fringes. Figs. 1f and 1g confirm the tight lattice contact between the (3−1−22) lattice plane (D-spacing=0.171 nm) of typical trigonal Ni_3Se_2 and the (−111) lattice plane (D-spacing=0.285 nm) of monoclinic $NiWO_4$. Energy dispersive X-ray spectroscopy (EDS) mapping profiles reveal the homogeneous distribution of Ni, W, Se, and O elements throughout the $Ni_3Se_2/NiWO_4$ sample (Fig. 1h). The water contact angle in Figure S4 reveals that the $Ni_3Se_2/NiWO_4$ displayed superior hydrophilicity with a contact angle of 0°. Such superhydrophilicity of $Ni_3Se_2/NiWO_4$ can optimize the adsorption strength of H_2O molecules on the active surface sites and enhance the catalytic performance [40,41]. Moreover, the inductively coupled plasma mass spectrometry (ICP-MS) analysis was used to further determine the detailed loading of different electrocatalysts. Thereinto, the $Ni_3Se_2/NiWO_4$ catalyst comprises 54.8 wt %/3.4 mg cm^{-2} W (Table S2). It is noteworthy that given that Ni serves

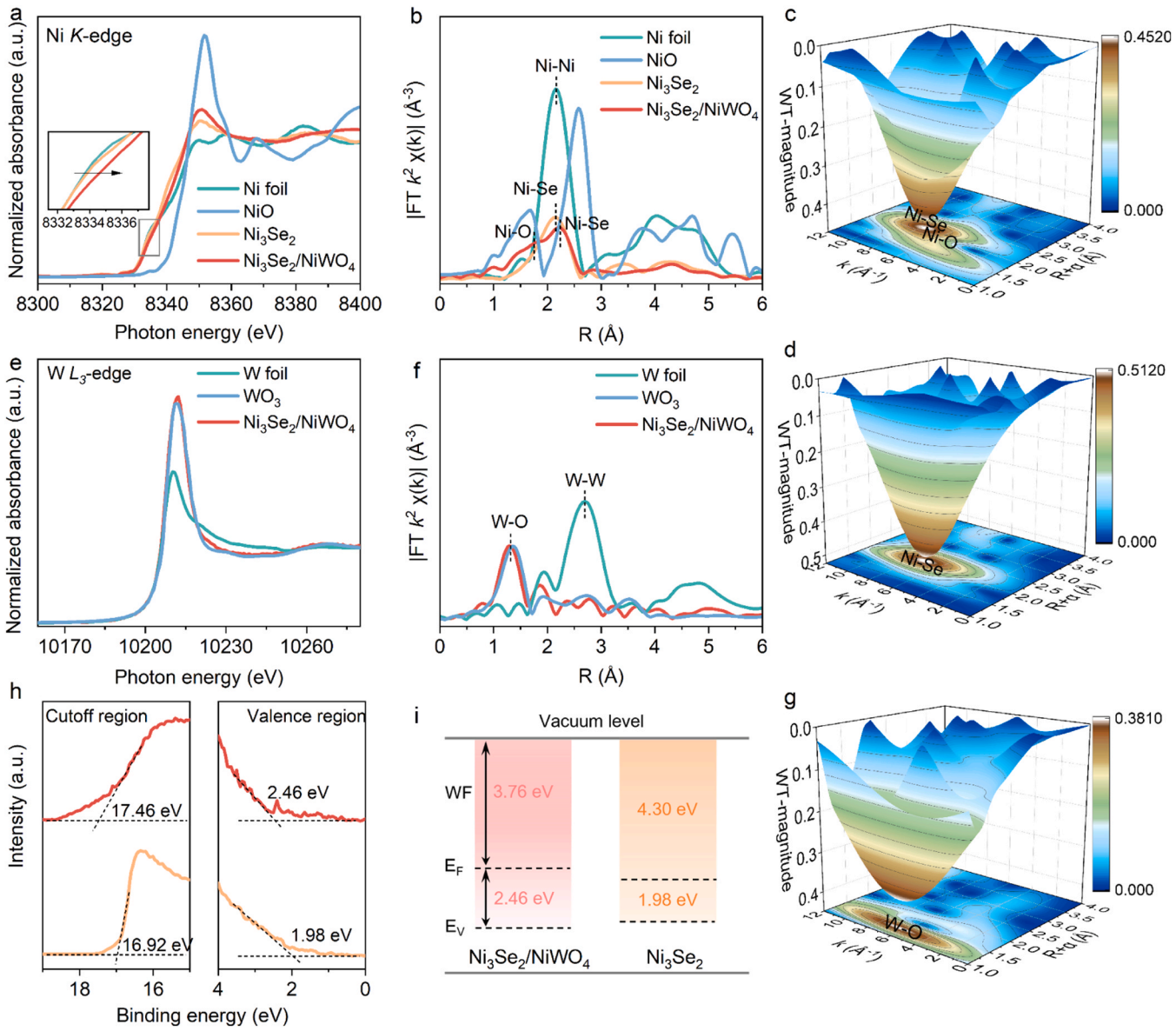

Fig. 2. (a) Ni *K*-edge, (b) Fourier transforms of k^2-weighted EXAFS spectra at Ni K-edge, and Wavelet-transformed k^2-weighted EXAFS spectra of (c) $Ni_3Se_2/NiWO_4$ and (d) Ni_3Se_2. (e) W L_3-edge XANES spectra, (f) Fourier transforms of k^2-weighted EXAFS spectra at W L_3-edge, and (g) Wavelet-transformed k^2-weighted EXAFS spectra of $Ni_3Se_2/NiWO_4$. (h) UPS spectra of $Ni_3Se_2/NiWO_4$ (up) and Ni_3Se_2 (down). (i) Band structure alignment of the $Ni_3Se_2/NiWO_4$ and Ni_3Se_2 catalysts.

as both a substrate and a Ni source, the determination of Ni loading is inaccurate.

X-ray photoelectron spectroscopy (XPS) was employed to investigate the chemical states and electronic interactions of the electrocatalysts. The XPS survey spectra, as depicted in Figure S5, confirm the coexistence of Ni, W, Se, and O elements in $Ni_3Se_2/NiWO_4$. As illustrated in Figure S6a, the high-resolution Ni 2*p* spectrum of the $Ni_3Se_2/NiWO_4$ exhibits distinct peaks at 853.48 and 871.08 eV, which can be attributed to Ni-Se bonds.The peaks at 855.30 and 872.84 eV originate from Ni-O bonds. Additionally, satellite peaks (abbreviated as Sat.) at 860.30 and 878.50 eV are discernible [42]. It is noteworthy that after introducing Lewis acid with an electron-withdrawing effect, the Ni peaks of $Ni_3Se_2/NiWO_4$ shifts toward higher binding energy compared with Ni_3Se_2, indicating W attracts electrons from Ni and a increase in the Ni valence state. The W 4 *f* XPS spectrum of $Ni_3Se_2/NiWO_4$ displays two peaks at 34.98 eV and 36.98 eV, which correspond well to the W $4f_{7/2}$ and W $4f_{5/2}$ of W^{5+} states, respectively (Figure S6b). The peaks at 35.70, 37.84, and 41.41 eV can be assigned to W^{6+} and WO_3 loss feature peak [43]. From the Se 3*d* spectrum of Ni_3Se_2 (Figure S6c), two differentiation of peaks at 53.35 and 54.27 eV corresponded to the Se $3d_{5/2}$ and Se $3d_{3/2}$ regions of the Ni-Se bond, respectively. The peak at 58.40 eV was assigned to the oxidized selenium species (SeO_x), which is inevitable in the air [44,45], Expectedly, the Se 3*d* spectrum of $Ni_3Se_2/NiWO_4$ shows weak signal with many burrs caused by the coverage of $NiWO_4$. In the O 1 *s* spectrum, it can be seen that three well-fitted peaks are well deconvoluted into the lattice oxygen (M-O) at 530.71 eV, surface hydroxyl groups bound to the metal ions (M-OH) at 531.72 eV, and surface-adsorbed water ($H_2O_{ads.}$) at 533.10 eV, severally (Figure S6d).

The chemical states of $Ni_3Se_2/NiWO_4$ and Ni_3Se_2 were analyzed using X-ray absorption near-edge spectroscopy (XANES). Fig. 2a displays the absorption edge of Ni *K*-edge XANES of $Ni_3Se_2/NiWO_4$ moves to higher energy compared to Ni_3Se_2, indicating a decrease in electron density on Ni atoms caused by the Lewis acid, in line with XPS results. The Ni *K*-edge extended X-ray absorption fine structure (EXAFS) of $Ni_3Se_2/NiWO_4$ (Fig. 2b) reveals clear peaks for Ni-O and Ni-Se bonding [46]. Remarkably, the relative positions of Ni-Se have obvious differences in the two samples, without phase correction, which is also

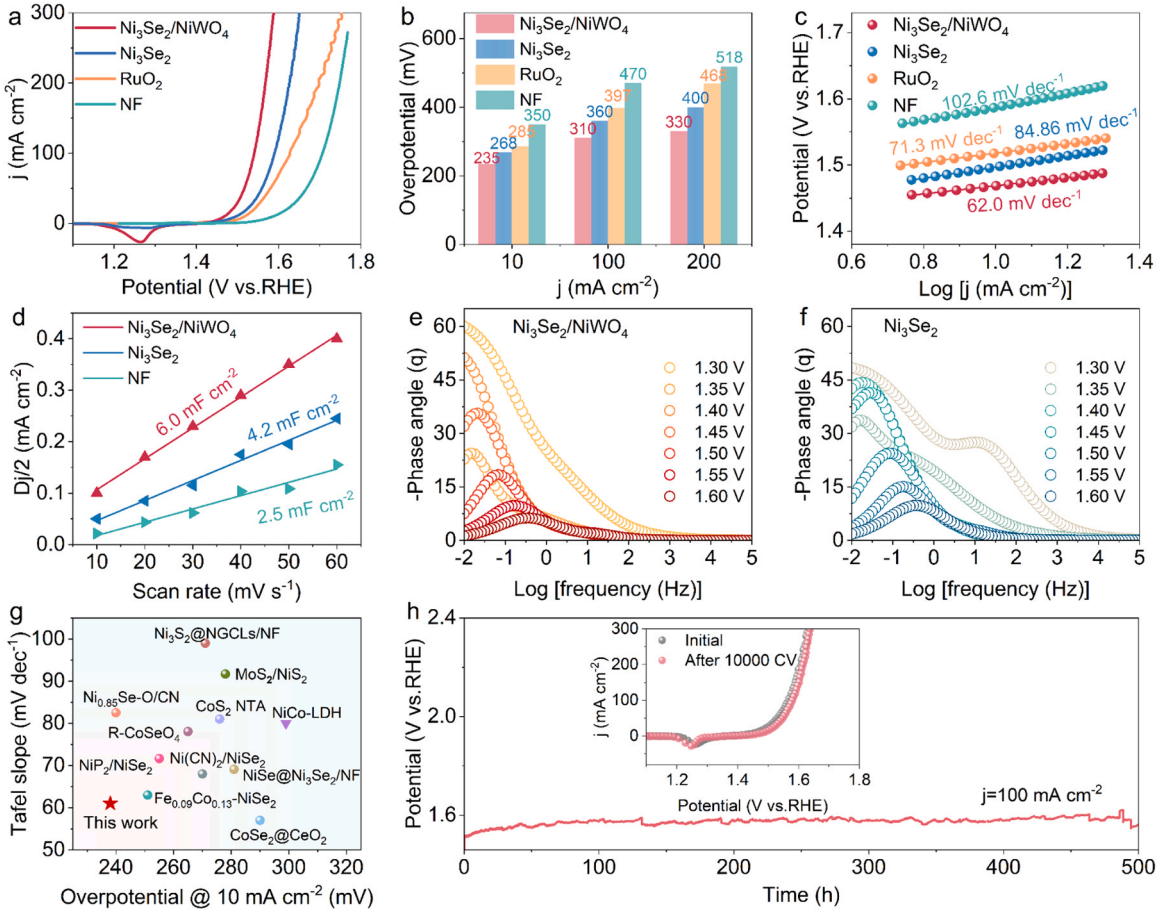

Fig. 3. (a) LSV polarization curves of $Ni_3Se_2/NiWO_4$, Ni_3Se_2, RuO_2 and NF catalysts. (b) Overpotentials at 10, 100, and 200 mA cm^{-2}. (c) Tafel plots. (d) C_{dl}. Bode phase plots of (e) $Ni_3Se_2/NiWO_4$ and (f) Ni_3Se_2. (g) Comparison with the recently reported catalysts. (h) Chronopotentiometric curve of $Ni_3Se_2/NiWO_4$ at 100 mA cm^{-2} (insets display the polarization curves of $Ni_3Se_2/NiWO_4$ before and after 10000 CV cycles).

confirmed by wavelet transform (WT) (Figs. 2c-2d and Figure S9). The model-based EXAFS fitting results of Ni *K*-edge EXAFS show that the coordination number of Ni-Se decreases from 3.7 (Ni_3Se_2) to 1.3 ($Ni_3Se_2/NiWO_4$) (Figure S7-S8 and Table S3). This change is attributed to the introduction of the 5*d* W stretching the bonding distance and forming low-coordination metal sites. The relatively high-valent Ni and the extended Ni-Se bond length are helpful for activating OER. Additionally, the W L_3-edge XANES spectrum indicates that the valence state of W in $Ni_3Se_2/NiWO_4$ approaches WO_3 (W^{6+}), exposing abundant *d*-band holes in W, which facilitates the reception of hydroxyl anions groups (Fig. 2e) [47]. The EXAFS spectra (Fig. 2f) and WT-EXAFS contour maps (Fig. 2g and Figure S10 and S11) exhibit a distinct peak at ≈ 1.36 Å (without phase correction), which corresponds to the first-shell W-O coordination.

Moreover, Ultraviolet photoelectron spectroscopy (UPS) shows lower work function in $Ni_3Se_2/NiWO_4$ (3.76 eV) than Ni_3Se_2 (4.30 eV), suggesting the electronic structure in $Ni_3Se_2/NiWO_4$ is modified due to charge redistribution between Ni_3Se_2 and $NiWO_4$ to reach the equilibrium state (Fig. 2h) [48]. The electronscan easily transfer from the inside of the catalyst to the surface for electron exchange with reactants after introducing the Lewis acid, W sites [49,50]. In addition, the UPS spectra displays a difference in valenceband maximum value, implying an altered electronic configuration in $Ni_3Se_2/NiWO_4$ (Fig. 2i) [51]. The above observations confirm that there is a strong electron interaction between Ni_3Se_2 and $NiWO_4$, which results in the change of activity around the interface and the regulation of catalyst's performance.

The electrochemical characteristics of $Ni_3Se_2/NiWO_4$, Ni_3Se_2, RuO_2 and NF catalysts were assessed in a 1.0 M KOH electrolyte. All polarization curves were recorded from high initial potential to low potential to prevent signal overlap of the oxidation peak. Linear sweep voltammetry (LSV) curves demonstrate that $Ni_3Se_2/NiWO_4$ composite exhibits significantly enhanced performance in the OER, displaying overpotentials of only 235, 310, and 330 mV at 10, 100, and 200 mA cm^{-2}, respectively, which are much lower than that observed for Ni_3Se_2 RuO_2, and NF catalysts (Figs. 3a and 3b). It suggested that the beneficial impact of $NiWO_4$ doping on enhancing the OER activity. Typically, the reduction peak is attributed to the Ni^{2+}/Ni^{3+} redox transition. Under anodic potentials, the $Ni_3Se_2/NiWO_4$ and Ni_3Se_2 undergoes electrochemical oxidation and surface reconstruction to form active NiOOH species, while the reduction peak in the reverse scan corresponds to the reduction of oxidized Ni species to lower-valence states (Figure S12). The more pronounced redox feature in $Ni_3Se_2/NiWO_4$ suggests facilitated Ni redox transformation, which promotes the formation of active species and enhances OER activity [52]. The reproducibility of the $Ni_3Se_2/NiWO_4$ synthesis was confirmed by performance data from three independent batches (Figure S13). Specifically, through systematic experiments contingent on different molar amounts of W^{6+}, we concluded that the most favorable OER performance is realized on $Ni_3Se_2/NiWO_4$ catalyst with 0.4 mmol W^{6+} (Figure S14). The OER activity follows a clear volcano-type trend with W content, where insufficient or excessive W dosage leads to reduced activity due to limited active sites or increased charge-transfer resistance, respectively. Although the complexity of the multiple OER steps makes it challenging to deduce the exact mechanism solely from the Tafel slope, the low value suggests favorable electrocatalytic kinetics. [53] $Ni_3Se_2/NiWO_4$ exhibits a lower Tafel slope (62.0 mV dec^{-1}) compared

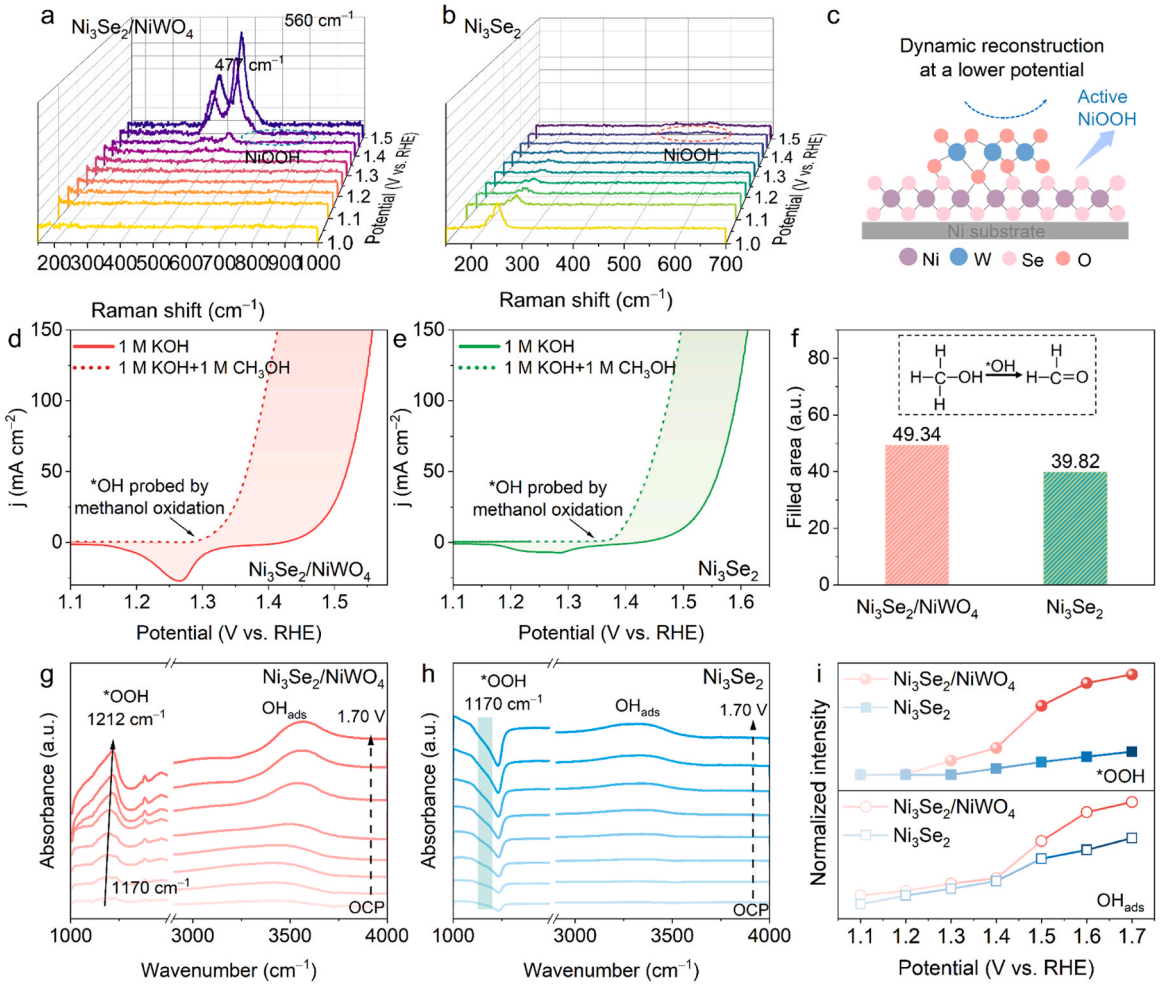

Fig. 4. *In-situ* Raman spectra at different potentials for (a) $Ni_3Se_2/NiWO_4$ and (b) Ni_3Se_2. (c) Schematic diagram of surface reconstruction. Polarization curves of (d) $Ni_3Se_2/NiWO_4$ and (e) Ni_3Se_2 in 1.0 M KOH solution with (dashed lines) and without (solid lines) 1.0 M methanol. (f) Current difference between the polarization curves in 1.0 M KOH solution with and without 1.0 M methanol for $Ni_3Se_2/NiWO_4$ and Ni_3Se_2. *In-situ* FTIR spectra of (g) $Ni_3Se_2/NiWO_4$ and (h) Ni_3Se_2. (i) Normalized peak intensity of *OOH and *OH as a function of applied potential for $Ni_3Se_2/NiWO_4$ and Ni_3Se_2.

to Ni_3Se_2 (84.86 mV dec^{-1}), RuO_2 (71.3 mV dec^{-1}), and NF (102.6 mV dec^{-1}), evidencing its rapid kinetic process (Fig. 3c). To evaluate the intrinsic activity of the catalysts, we determined the electrochemically active surface area (ECSA) through measurements of the double-layer capacitance (C_{dl}). $Ni_3Se_2/NiWO_4$ delivers higher C_{dl} (6.0 mF cm^{-2}) and ECSA (150 cm^2) than other catalysts (Fig. 3d, Figure S15 and Figure S16a), indicating much more exposed active sites after introducing $NiWO_4$. ECSA-normalized LSV is conducted to further investigate the intrinsic activity of the catalysts. As illustrated in Figure S16b, $Ni_3Se_2/NiWO_4$ exhibits the highest ECSA-normalized current density. Besides, the ECSA-normalized current density for $Ni_3Se_2/NiWO_4$ achieved 0.5 mA cm^{-2}, at the overpotential of 300 mV, which was about 2-fold higher than those for Ni_3Se_2 (0.25 mA cm^{-2}). The turnover frequency (TOF) values, also demonstrates the best performance of $Ni_3Se_2/NiWO_4$, with the TOF value of 0.0065 s^{-1} at η= 300 mV, much higher than that of Ni_3Se_2 (0.0041 s^{-1}) (Figure S16c-d) [54]. These trend for the tested samples aligns with the LSV results, indicating the high activity of $Ni_3Se_2/NiWO_4$ catalyst not only from the larger active area, but also the enhanced intrinsic activity [55]. As illustrated in Figure S17 and S18, the Faradaic efficiency (FE) for $Ni_3Se_2/NiWO_4$ demonstrated close to 100%, as determined by comparing the experimentally obtained oxygen volume with the theoretical expectation. The *in-situ* EIS tests were performed at different applied potentials (1.30 – 1.60 V vs. RHE) to further understand the electrochemical reaction kinetics process. With increasing potential, the semicircle observed in the Nyquist plots diminishes significantly, indicative of faster reaction kinetics and more efficient adsorption of reactants. The lowest R_{ct} value and the most rapid decrease in R_{ct} for $Ni_3Se_2/NiWO_4$ indicate its superior kinetics for adsorbing key oxygen-containing intermediates and its good ability to adsorb reactants at a lower driving potential (Figure S19 and Table S4). To further investigate the kinetics of the electrochemical reaction process, the phase angle vs. voltage plots is shown in Fig. 3e and f. In the EIS-derived Bode phase plots, the peak in the high-frequency range (10^2 – 10^5 Hz) is associated with the oxidation of electrocatalysts, while the peak in the low-frequency range (10^{-2}– 10^1 Hz) is indicative of OER process [56]. Upon increasing the applied potentials, the smaller phase peak angle was observed for $Ni_3Se_2/NiWO_4$ in the low-frequency region compared that of Ni_3Se_2, signifying that the interaction at the interface between the catalyst and the electrolyte facilitates the charge-transfer process, thus improving the kinetics of the OER. A comparison of the overpotential and Tafel slope with previously reported non-precious catalysts is depicted in Fig. 3g and summarized in Table S5, which confirm the superior performance and kinetics of $Ni_3Se_2/NiWO_4$ catalyst. Apart from the excellent activity, the long-term durability of the catalyst is another vital indicator. The OER stability of the as-prepared $Ni_3Se_2/NiWO_4$ was evaluated by continuous cyclic CV for 1000 cycles and chronopotentiometry (CP) test at constant current densities of 100 mA cm^{-2}. As shown in the inset of Fig. 3h, no obvious decay in polarization curves was observed for $Ni_3Se_2/NiWO_4$ after 10000 cycles. Furthermore, the overpotential required to achieve the

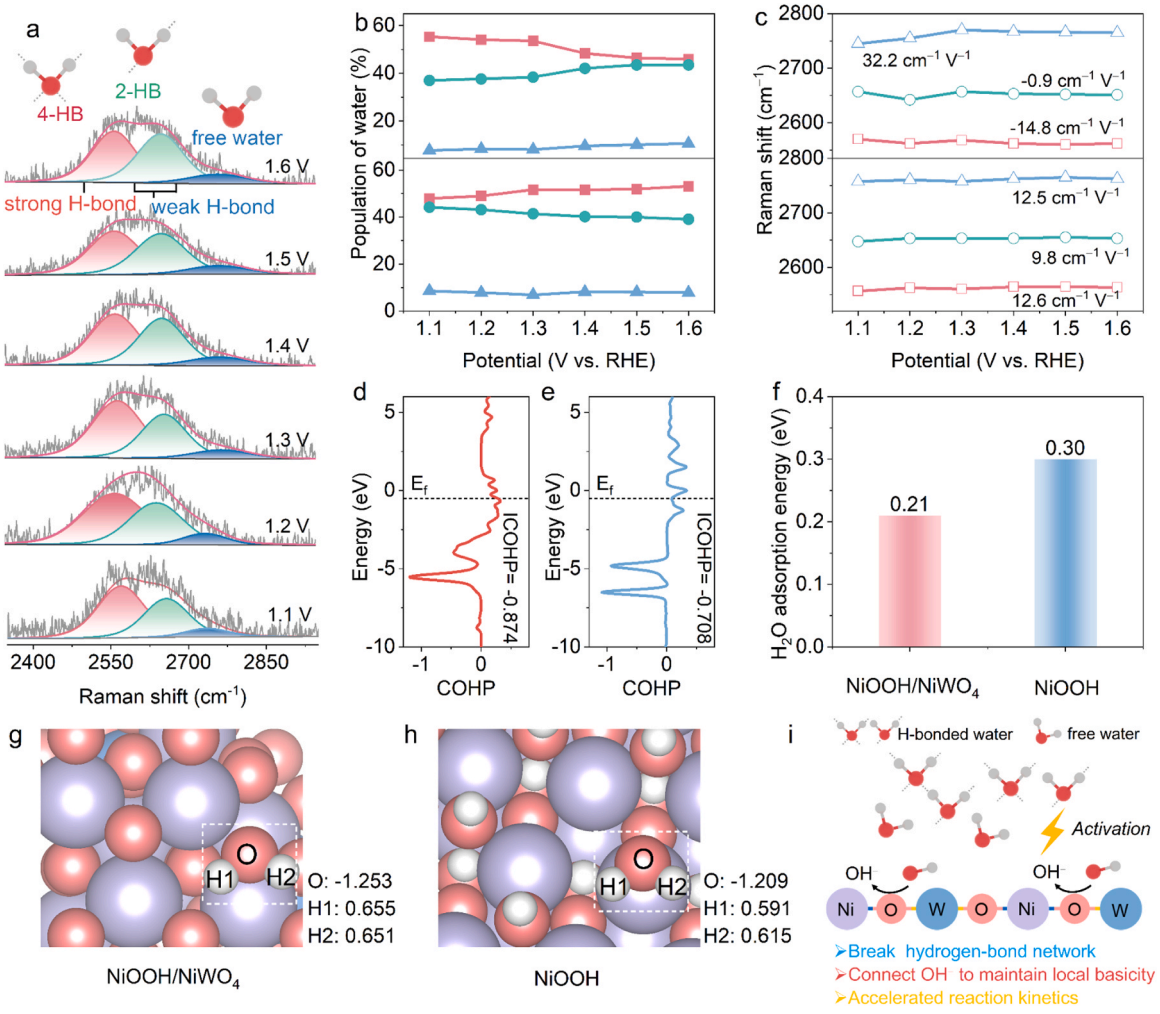

Fig. 5. (a) Potential-dependent absorption intensities of interfacial water measured by *in-situ* Raman in the1 M KOH electrolyte for $Ni_3Se_2/NiWO_4$. (b) The population of different types of water on $Ni_3Se_2/NiWO_4$ (up) and Ni_3Se_2 (down). (c) Potential-dependent peak shifts of various interfacial water types in $Ni_3Se_2/NiWO_4$ (up) and Ni_3Se_2 (down). ICOHP between chemisorbed H_2O and Ni active centers on (d) $NiOOH/NiWO_4$ and (e) NiOOH. (f) Calculated H_2O adsorption energy. Charge state of the H and O atoms on (g) $NiOOH/NiWO_4$ and (h) NiOOH. (i) Schematic representation of the electrochemical interface during water oxidation.

current density of 100 mA cm^{-2} remained constant with a negligible increase over 500 h, suggesting its good durability (Fig. 3h). As a binder-free electrode, the as-synthesized $Ni_3Se_2/NiWO_4$ exhibits good activity and durability under alkaline conditions as concluded above.

The electrochemical *in-situ* Raman spectroscopy was employed to probes the catalyst structural evolution and interface local environments (The catalysts were not subjected to CV activation as for LSV measurements). Apparently, the peaks located at around 246 cm^{-1} can be indexed to nickel selenides [57,58], which are not observable in $Ni_3Se_2/NiWO_4$ catalyst due to $NiWO_4$ effectively obscuring the associated Raman signal during the second reaction step, align with Se 3*d* XPS results. A weak W-O peak of $NiWO_4$ at ~810 cm^{-1} is visible in Figure S20. Its intensity diminishes with increasing potential due to the accumulation of surface NiOOH species, which obscure the Raman signal from the underlying $NiWO_4$. [59] As the potential increased, new coupled E_g (bending vibration of the oxygen atoms along the plane) and $A_{1\,g}$ (stretching vibration of oxygen atom perpendicular to the plane) bands appeared at 477 and 560 cm^{-1}, which are attributed to Ni-O bond in NiOOH (Figs. 4a and 4b) [60,61]. Notably, the formation of NiOOH species, active for $Ni_3Se_2/NiWO_4$ catalyst at a lower potential (1.35 V) compared to Ni_3Se_2 (1.45 V), demonstrates that incorporating $NiWO_4$ significantly contributes to dynamic reconstruction, thus improving the catalytic activity. Moreover, compared to Ni_3Se_2, the peak intensity of NiOOH species in $Ni_3Se_2/NiWO_4$ catalyst became more prominent as the potential increased from 1.35 V to 1.50 V, suggesting that a higher population of the active species was formed. *In-situ* Raman spectroscopy confirms that Lewis acid sites are instrumental to lower the generation potential of active species while increasing quantity (Fig. 4c). The reduced formation potential of NiOOH is attributed to the synergistic effects of the electron-withdrawing modulation of W^{6+} centers and $Ni_3Se_2/NiWO_4$ interfacial coupling, which facilitate charge transfer and lower the $Ni^{2+}\rightarrow Ni^{3+}$ oxidation barrier, together with the formation of a locally OH^--enriched microenvironment that thermodynamically promotes the transformation.

Under alkaline conditions for OER, the redox of active sites is typically coupled with the transfer of hydroxide ions (OH^-). The adsorption behavior of hydroxyl species on the catalysts is investigated using Zeta potential measurement, which reflects the charge density of the catalyst's surface and provides insights into the interaction between the catalysts and OH species [23]. Lewis acid exhibits negative charge accumulation at the catalyst−electrolyte interface to resist the rapid and persistent depletion of OH^- during OER. [30] As shown in Figure S21, $Ni_3Se_2/NiWO_4$ exhibits optimized adsorption of OH^-, with a more negative potential of −16.0 mV compared to Ni_3Se_2 (−5.84 mV). This is attributed to the introduction of a Lewis acid layer (tungstate) on the catalyst surface to capture a huge amount OH^- surrounding the catalyst [29]. Meanwhile, monitoring the pH near the electrode surface reveals a slightly higher local pH for $Ni_3Se_2/NiWO_4$, indicating OH^- enrichment

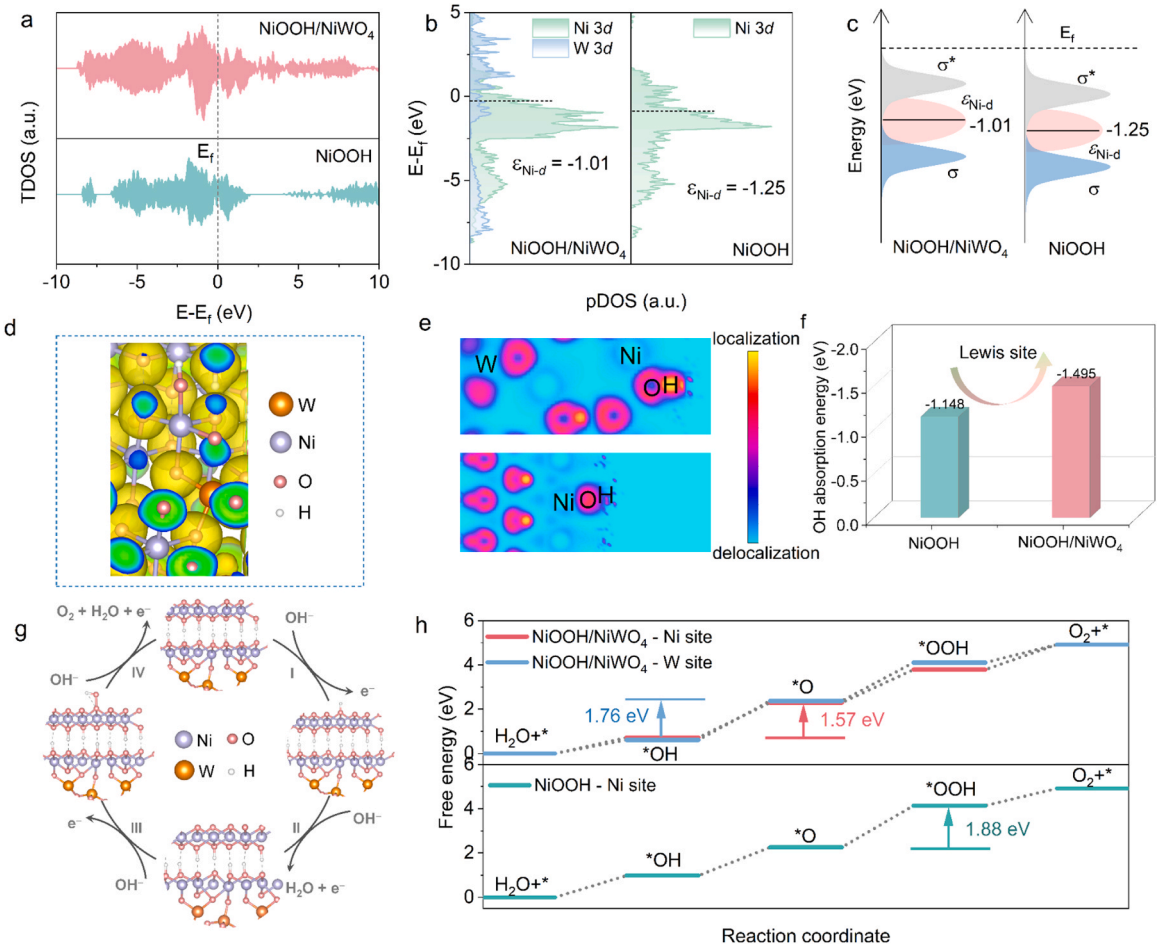

Fig. 6. (a) The DOS plots and (b) pDOS plots for $NiOOH/NiWO_4$ and NiOOH. (c) Schematic d-band diagrams. The bonding and antibonding states are indicated by σ and σ*, respectively. (d) ELF of $NiOOH/NiWO_4$. (e) Evaluation of OH adsorption using the ELF and (f) the OH adsorption energy for $NiOOH/NiWO_4$ and NiOOH. (g) The proposed alkaline OER mechanism on $NiOOH/NiWO_4$. (h) OER free-energy diagrams for $NiOOH/NiWO_4$ and NiOOH.

induced by the Lewis acidic W species (Figure S22). Due to the existence of such generated local alkalinity, such preferential enrichment of OH^- is effectively manifested in the enhanced first reaction intermediate (*OH) during the OER process ($* + OH^- \rightarrow *OH + e^-$). [62] The strengthened *OH adsorption was also experimentally confirmed using methanol as a probe. The methanol oxidation reaction (MOR) follows a well-established mechanism where methanol molecules nucleophilically attack the electrophilic *OH. Consequently, MOR is more active on surfaces with stronger *OH adsorption [63]. Upon introducing 1.0 M methanol into a 1.0 M KOH solution, the current densities for both $Ni_3Se_2/NiWO_4$ and Ni_3Se_2 increased significantly (Figs. 4d and 4e), attributable to methanol electrooxidation. The difference in current densities, directly proportional to the number of transferred charges, was quantified by calculating the area between the curves [64]. Notably, compared to Ni_3Se_2, a larger current difference observed for $Ni_3Se_2/NiWO_4$ decorated by Lewis acid sites between the MOR versus OER (Fig. 4f), indicates stronger MOR competition, verifying enhanced *OH adsorption. Next, we perform *in-situ* Fourier transform infrared (FTIR) spectroscopy to monitor surface oxygen intermediates on the catalyst during OER using a custom-made electrochemical cell. Upon applying potential, distinct peaks were detected at 1212 cm^{-1} for $Ni_3Se_2/NiWO_4$ and 1170 cm^{-1} for Ni_3Se_2 (Figs. 4g and 4h), which represents the stretching vibration of the *OOH species, consistent with the characteristics of the typical adsorption evolution mechanism (AEM) [65,66]. The *in-situ* IR spectra show a positive shift of the *OOH peak from 1170 cm^{-1} (Ni_3Se_2) to 1212 cm^{-1} ($Ni_3Se_2/NiWO_4$). This shift arises from the Lewis acid reducing the electron density of active Ni sites and strengthening the O-O bond of adsorbed *OOH. Such optimization enhances intermediate adsorption and accelerates kinetics. [67] Most noticeably, the peak intensity of *OOH recorded on $Ni_3Se_2/NiWO_4$ is considerably stronger than that for Ni_3Se_2, which confirms the incorporation of Lewis acid sites supplies the necessary reactants for the conversion from *O to *OOH, thereby facilitating the subsequent reactions and oxygen exchange [68]. Previous studies have shown that the formation of *OOH is generally considered to be the rate-determining step (RDS) [69,70]. It is inferred that the enrichment of *OOH intermediates in $Ni_3Se_2/NiWO_4$ implies a change and decrease in the free energy of RDS during the OER process, which will be further confirmed in subsequent discussion. Meanwhile, the wavenumbers ranging from 3200 to 3600 cm^{-1} are attributed to the O—H stretching mode of OH^-. The increase in OH^- vibration intensity on $Ni_3Se_2/NiWO_4$ is higher than that on Ni_3Se_2, indicating that abundant OH^- can be adsorbed on the surface of $Ni_3Se_2/NiWO_4$. [71] The above results consistently suggest that interface in $Ni_3Se_2/NiWO_4$ effectively promotes adsorbed OH^- to participate in the anodic reaction (Fig. 4i). Besides, higher wavenumbers indicate weakened hydrogen bonding, resulting in enhanced mobility of interfacial water [47]. Interestingly, compared to Ni_3Se_2, a distinct shift toward higher wavenumbers with increasing potential is observed in the $Ni_3Se_2/NiWO_4$ peaks, indicating a greater proportion of free water on the catalyst surface. Therefore, the introduction of Lewis acids facilitates the enrichment of interfacial water, which is consistent with predictions from *in-situ* Raman results.

We used *in-situ* Raman spectroscopy to investigate the supramolecular interactions of interfacial water molecules under varying potentials,

shedding light on their molecular-level activation mechanism and its determinant role in the water molecules' reactivity during subsequent OER steps. A broad band spanning over the wavenumber range of 2000–3000 cm^{-1}, which is attributed to the OH stretching mode, appears in both $Ni_3Se_2/NiWO_4$ and Ni_3Se_2. The OH stretching band was resolved into three distinct components through Gaussian deconvolution, each representing a unique hydrogen-bonding configuration of interfacial water. Specifically, the 4-coordinated H-bonded water (4HB-H_2O) belongs to strong H-bonded water, while the 2-coordinated H-bonded water (2HB-H_2O) and the cation (K^+ in our electrolyte system) hydrated water (K-H_2O) correspond to weak H-bonded water [72,73]. Interestingly, these components show different evolution trends in response to increasing potentials in the two catalysts. The proportion of 2HB-H_2O and K-H_2O in $Ni_3Se_2/NiWO_4$ demonstrate a growth with the applied potential increasing from 1.1 to 1.6 V (Figs. 5a and 5b), while 4HB-H_2O showed a decreasing trend. For the Ni_3Se_2, the 4HB-H_2O signal exhibits a gradual increase (Figure S23). The Stark slope, derived from the linear plot of vibration frequency against electrode potential, quantified the contribution of each water component. A steeper Stark slope indicates that free H_2O is more sensitive to local electric fields than 4-HB-H_2O and 2-HB-H_2O (Fig. 5c). Following the classical Grotthuss mechanism, the migration of OH is contingent upon hydrogen bonds network [25]. These results suggest that the Lewis acid restructures the interfacial water molecules into a dynamic and flexible hydrogen-bonded network, which facilitates the transport of OH^- ions and makes it easier to activate electrochemically for the subsequent OER steps.

Through the analysis of bonding and antibonding orbital filling [74,75], the crystal orbital Hamilton population (COHP) and integrated COHP (ICOHP) calculations results demonstrate that $NiOOH/NiWO_4$ exhibits the lowest ICOHP value (−0.874), indicating a stronger H_2O-M interaction compared to NiOOH (−0.708), as shown in Figs. 5d and 5e. Further calculation of the H_2O adsorption energy revealed that introducing Lewis acid sites enhanced water adsorption, thereby modulating the hydrogen-bond network (Fig. 5f). In addition, the Bader charge analysis of $*H_2O$ on $NiOOH/NiWO_4$ shows that enhanced the polarization of the O-H bonds, which effectively drives the reorganization of hydrogen-bond network structure (Figs. 5g and 5h). These results reveal that the Lewis acid induces dynamic transformation of the rigid the hydrogen-bond network, thereby increasing the interfacial water content and thus the concentration of active OH species, which provides a prerequisite for sustained OER (Fig. 5i).

Based on *in-situ* electrochemical Raman and IR results, the structure of $Ni_3Se_2/NiWO_4$ after stability was further investigated. The SEM of post-stability (Figure S24) reveals slight agglomeration in the surface morphology, which is inevitable in the continuous operation. The Ni 2*p* XPS spectrum after stability indicates a markedly increased ratio of Ni^{3+}/Ni^{2+}, suggesting the oxidation of Ni^{2+} with the formation of active NiOOH (Figure S25a). Notably, Figure S25b shows minimal signals associated with Se atoms, indicating nearly complete leaching of Se, consistent with previous reports [76,77]. The cleavage of the Ni–Se bonds and the leaching of Se lead to a rearrangement of the electronic structure at the metal center, consequently enhancing the activity of the derived-NiOOH [60]. The shift of W 4*f* XPS to lower binding energy indicates an increase in electron cloud density of W, which further confirms the electron acceptor characteristic of Lewis acid (Figure S25c). The above results indicate that the surface of the catalyst underwent a reconfiguration into a metal hydroxide beneficial for OER.

Density functional theory (DFT) calculations were performed to better understand the regulation mechanism of the Lewis acid on OER activity at active Ni sites. The corresponding atomic models, based on the conclusion of surface reconstruction, are shown in Figure S26. The (105) facet of NiOOH and (-111) facet of $NiWO_4$ were adopted as the crystal surfaces for DFT calculations. The total density of states (TDOS) calculation shows that $NiOOH/NiWO_4$ has greater density of states at the Fermi energy (E_f) level, suggesting improved conductivity and explaining its exceptional activity (Fig. 6a). The projected density of state (PDOS) illustrates that Ni *d*-orbital electrons contributions are mainly in the valence band, whereas the conduction band is composed predominantly W *d*-orbital electrons (Fig. 6b). This analysis preliminarily indicated that Ni serves as catalytic active sites by contributing the states near the valance band edge [78]. Compared with NiOOH (−1.25 eV), the calculated Ni *d*-band center (ε_d) of $NiOOH/NiWO_4$ (−1.01 eV) is significantly raised owing to the electronic transference. According to the *d*-band theory, the upshifted *d*-band center may lead to the enhanced adsorption of oxygen-containing intermediates at the Ni site. Further analysis of the abundance of *d*-orbital electrons close to the Fermi level, rather than significantly below it, enables the efficient charge transfer from transition metals centers to oxygenated intermediates during the OER process (Fig. 6c) [79]. After a rounded analysis, it is clear that the model architecture harbors promising active sites denoted as Ni-O-W-O-Ni and Ni-O-Ni-O-Ni. The electron localization function (ELF) can intuitively display the charge distribution state of W atoms. The results show that the charge is obviously enriched around W atom (yellow regions indicate charge accumulation). This observation is fully consistent with the electron-accepting behavior of W revealed by XPS characterization, further clarifying the electronic modulation effect of Lewis acid sites on the catalytic interface (Fig. 6d). W regulates electrons redistribution through Ni-O-W bonds, regulating the surface charge distribution of high-active NiOOH through interfacial interactions [47].

As proven by the above Zeta potential and *in-situ* characterizations experiments, the Lewis acid sites can enhance the OH adsorption. The ELF analysis was further employed to evaluate OH adsorption on NiOOH and $NiOOH/NiWO_4$. A color-scale scheme was employed to elucidate the ELF, in which yellow stands for a fully localized state and blue stands for a fully delocalized state. It reveals that electron localization by the Ni-bound OH was enhanced after introducing W (Fig. 6e). It is also confirmed by the theoretical calculated results that the OH adsorption energy for $NiOOH/NiWO_4$ is −1.495 eV, more negative than that of −1.148 eV for pure NiOOH (Fig. 6f). The increased OH^- adsorption facilitates the surface phase transformation of selenides to hydroxide and OER-active oxyhydroxide. Therefore, theoretical calculations confirm that introducing Lewis acid sites on Ni sites can regulate hydroxyl connectivity, which is beneficial for driving the subsequent process forward.

To identify the OER mechanism featured by our catalysts, we carried out OER tests in the presence of tetramethylammonium hydroxide (TMAOH), as tetramethylammonium cations (TMA^+) can selectively bind to adsorbed peroxide, a key intermediate of lattice oxygen oxidation mechanism (LOM). [80] By simply using 1.0 M TMAOH as the electrolyte, we witnessed that both $Ni_3Se_2/NiWO_4$ and Ni_3Se_2 remained almost unaffected, confirming mainly follows the AEM (Figure S27). Furthermore, as expected from the Raman spectra (Figure S28), there are no the characteristic peaks of TMA^+, when the two electrodes were operated at a constant potential of 1.55 V versus RHE in 1.0 M TMAOH electrolyte. These results validate that the two catalysts undertake an AEM pathway. [81] The OER was proposed to follow a four-electron transfer pathway involving the sequential formation of adsorbed *OH, *O, and *OOH intermediates (where asterisks denote adsorption sites) (Fig. 6g, Figure S29 and S30). The Gibbs free energy changes also calculated for each elementary step in the OER, which based on the free energy of the rate-determining step (RDS). As shown in Fig. 6h, the W sites in $NiOOH/NiWO_4$ exhibit the lowest OH adsorption energy ($\Delta G_1 =$ 0.61 eV), indicating the strong adsorption of OH, which confirms the its Lewis acidity. This causes a significant activation energy barrier for OH desorption and O-O coupling on the W sites, consequently leading to the weak OER activity. The Ni sites in $NiOOH/NiWO_4$ exhibit favorable thermodynamic energy barrier than that of W sites, indicating that the Ni sites are the main active centers for OER. The formation of *OOH from *O is the RDS for NiOOH, and its free energy barrier (1.88 eV) is higher than that for $NiOOH/NiWO_4$ (1.49 eV) (Table S7). Nevertheless,

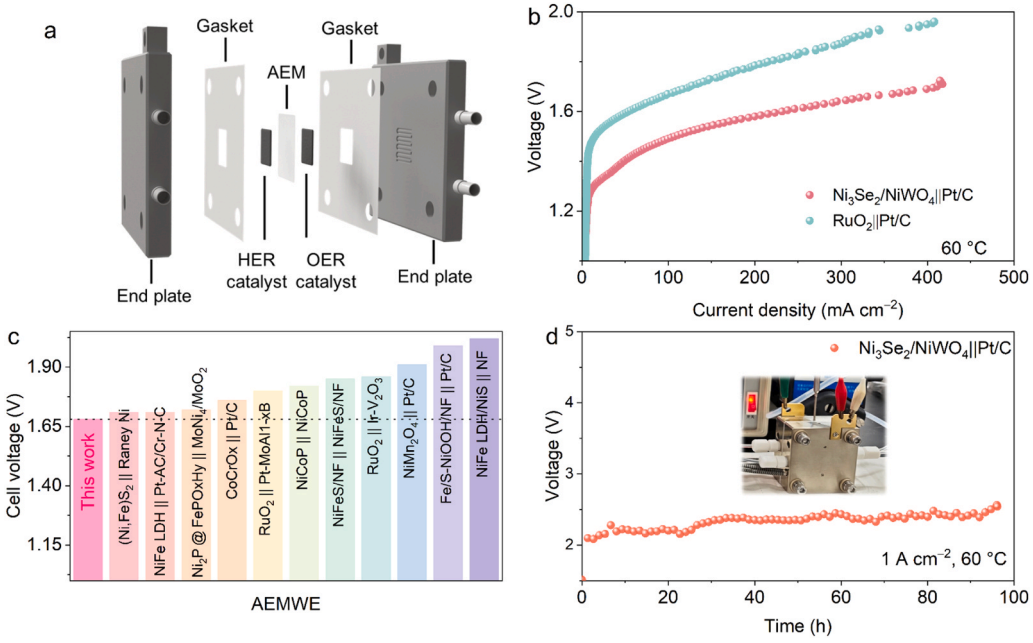

Fig. 7. (a) Schematic of the AEMWE device. (b) Polarization curves at 60 °C in 1.0 M KOH. (c) Performance comparison of recent reported bifunctional catalysts based AEMWE. (d) The long-term durability of Ni_3Se_2/$NiWO_4$||Pt/C was measured at a constant current density of 1 A cm^{-2} at 60 °C.

the RDS for NiOOH/$NiWO_4$ from *OOH formation to *O formation, and the free energy barrier decreased drastically to 1.57 eV, suggesting that the OER activity of NiOOH/$NiWO_4$ can be indeed enhanced by activating *OOH intermediates, in line with *in-situ* FTIR results. This result indicates predominant active site for the OER was identified as the Ni-O-W-O-Ni site. This site is proposed to enable a W led efficient site, which supports the activation and stabilization of *OOH intermediates. Consequently, our modified OER mechanism involves the accelerated formation and increased coverage of *OOH intermediates on the catalyst surface via the hydroxyl (Lewis base) captured by W sites, which lowers the energy barrier of RDS in conventional AEM and greatly increases the catalytic effectiveness.

Given such an excellent OER performance, we constructed an alkaline anion-exchange membrane water electrolyzer (AEMWE) using Ni_3Se_2/$NiWO_4$ as the anode and commercial Pt/C spray-deposited on carbon paper as the cathode, aiming to approximate industrial water electrolysis conditions (Fig. 7a). As shown in Fig. 7b, the noble metal-free AEMWE device with a Ni_3Se_2/$NiWO_4$ anode exhibits a lower cell voltage than that of the RuO_2-based device. In terms of current density performance, the Ni_3Se_2/$NiWO_4$-based noble metal-free electrolyzer surpasses most previously reported noble metal-free AEMWE systems at the current density of 400 mA cm^{-2}, as illustrated in Table S7 and Fig. 7c, indicating its application in future green hydrogen production. Moreover, the cell voltage of Ni_3Se_2/$NiWO_4$||Pt/C exhibits outstanding long-term durability at 1.0 A cm^{-2} for 96 h in AEMWE (Fig. 7d).

4. Conclusions

In summary, we incorporate a Lewis acid tungstate layer onto Ni_3Se_2 catalyst to deliberately control the local alkalinity of the interfacial microenvironment to improve water oxidation effectively. Detailed *in-situ* spectroscopic evaluations and theoretical calculations elucidate an efficient catalytic mechanism: Lewis acid binds OH^- (hard Lewis base) and restructures the interfacial hydrogen-bond network to generate a localized, sustained alkaline micro-environment at active Ni sites. This engineered interface ensures continuous OH^- supply and stabilizes active intermediates during OER process. As expected, the well-designed Ni_3Se_2/$NiWO_4$ composite achieves a reduced overpotential of 235 mV at 10 mA cm^{-2} in alkaline electrolyte and stable activity for 500 h at 100 mA cm^{-2}. The Ni_3Se_2/$NiWO_4$ exhibits remarkable durability in an AEMWE system, maintaining an industrial-grade current density of 1 A cm^{-2} for 96 h. This study provides a promising strategy for establishing surface microenvironment to rationally and accurately design highly active OER electrocatalysts, which broadens applications in exploring other electrocatalytic reactions.

CRediT authorship contribution statement

Fengli Wei: Writing – original draft, Methodology, Investigation, Conceptualization. **Jinghao Shen:** Methodology, Investigation. **Zuyang Luo:** Methodology, Investigation. **Panpan Sun:** Methodology, Investigation, Conceptualization. **Heyang Liu:** Data curation. **Xiaofeng Shi:** Formal analysis. **Bo Liu:** Software. **Dapeng Cao:** Conceptualization, Formal analysis. **Zhenbo Wang:** Conceptualization, Supervision. **Bin Wu:** Writing – review & editing, Supervision, Methodology, Investigation, Funding acquisition, Formal analysis, Data curation, Conceptualization. **Xiulin Yang:** Writing – review & editing, Supervision, Methodology, Investigation, Funding acquisition, Conceptualization. **Yongfa Zhu:** Writing – review & editing, Visualization, Methodology, Investigation, Conceptualization.

Declaration of Competing Interest

The authors declare that they have no known competing financial interests or personal relationships that could have appeared to influence the work reported in this paper.

Acknowledgements

This work was financially supported by the Guangxi Science and Technology Projects (GUIKE LT2600640010), the National Natural Science Foundation of China (52363028), the Natural Science Foundation of Guangxi Province (2021GXNSFAA076001), the Guangxi Technology Base and Talent Subject (GUIKE AD23023004, GUIKE AD20297039), the National Research Foundation, Singapore, and A*STAR (Agency for Science, Technology and Research) under its LCER Phase 2 Programme 1st Emerging Technology (Award No. U2411D4006), the National Research Foundation, Singapore, under its

Frontier Competitive Research Programme (NRF-F-CRP-2024-0008). We thank Shenzhen HUASUAN technology Co, Ltd. for assistance on theoretical calculations.

Appendix A. Supporting information

Supplementary data associated with this article can be found in the online version at doi:10.1016/j.apcatb.2026.126821.

Data availability

Data will be made available on request.

References

[1] R. Wang, Q. Kang, R. Wang, Q. Zong, L. Yan, X. Meng, F. Chang, T. Ma, C. Jin, Understanding the key factors in high entropy electrocatalysts for an efficient oxygen evolution reaction, J. Energy Chem. 110 (2025) 788–822.

[2] L. Wu, M. Ning, X. Xing, Y. Wang, F. Zhang, G. Gao, S. Song, D. Wang, C. Yuan, L. Yu, J. Bao, S. Chen, Z. Ren, Boosting oxygen evolution reaction of (Fe,Ni)OOH via defect engineering for anion exchange membrane water electrolysis under industrial conditions, Adv. Mater. 35 (2023) 2306097.

[3] H.S. Chavan, C.H. Lee, A.I. Inamdar, J. Han, S. Park, S. Cho, N.K. Shreshta, S. U. Lee, B. Hou, H. Im, H. Kim, Designing and tuning the electronic structure of nickel-vanadium layered double hydroxides for highly efficient oxygen evolution electrocatalysis, ACS Catal. 12 (2022) 3821.

[4] Y. Wu, G. Xu, J. Zhou, D. Cao, Research progress of the porous membranes in alkaline water electrolysis for green hydrogen production, Chem. Eng. J. 505 (2025) 159291.

[5] M. Xing, S. Zhu, X. Zeng, S. Wang, Z. Liu, D. Cao, Amorphous/crystalline $Rh(OH)_3$/CoP heterostructure with hydrophilicity/aerophobicity feature for all-pH hydrogen evolution reactions, Adv. Energy Mater. 13 (2023) 2302376.

[6] G. Xu, M. Xing, Z. Qiao, M. Han, Y. Wu, S. Wang, D. Cao, Constructing ultra-stable electrocatalysts to achieve adaptability of industrial-level alkaline water electrolyzers for fluctuating renewable energies, Adv. Energy Mater. 15 (2025) 2500926.

[7] Q. Ji, B. Tang, X. Zhang, C. Wang, H. Tan, J. Zhao, R. Liu, M. Sun, H. Liu, C. Jiang, J. Zeng, X. Cai, W. Yan, Operando identification of the oxide path mechanism with different dual-active sites for acidic water oxidation, Nat. Commun. 15 (2024) 8089.

[8] N. Zhang, X. Feng, D. Rao, X. Deng, L. Cai, B. Qiu, R. Long, Y. Xiong, Y. Lu, Y. Chai, Lattice oxygen activation enabled by high-valence metal sites for enhanced water oxidation, Nat. Commun. 11 (2020) 4066.

[9] P. Sun, Z. Qiao, X. Dong, R. Jiang, Z. Hu, J. Yun, D. Cao, Designing 3d transition metal cation-doped $MRuO_x$ as durable acidic oxygen evolution electrocatalysts for PEM water electrolyzers, J. Am. Chem. Soc. 146 (2024) 15515–15524.

[10] M. Xing, Z. Qiao, S. Zhu, G. Xu, J. YUn, D. Cao, Zipper-like interlocked heterostructure of NiFe layered double hydroxide-WN for super-stable oxygen evolution over 4500h, Adv. Funct. Mater. 34 (2024) 2409559.

[11] B.-C. Shi, M. Jin, Y. Zou, S. Wang, Y. Nie, D. Yao, Y.-J. Tang, Cathodic electrodeposition activation of NiFe-based metal-organic frameworks for enhanced oxygen evolution reaction, Rare Met. (2025).

[12] N. Wen, H. Wang, Q. Liu, K. Song, X. Jiao, Y. Xia, D. Chen, Field-effect enhancement of non-faradaic processes at interfaces governs electrocatalytic water splitting activity, Adv. Sci. 11 (2024) 2403206.

[13] Z. Li, X. Wu, X. Jiang, B. Shen, Z. Teng, D. Sun, G. Fu, Y. Tang, Surface carbon layer controllable Ni_3Fe particles confined in hierarchical N-doped carbon framework boosting oxygen evolution reaction, Adv. Powder Mater. 1 (2022) 100020.

[14] Z.-J. Zhang, J.-P. Guo, S.-H. Sun, Q. Sun, Y.-W. Zhao, Y.-F. Zhang, Z.-Y. Yu, C.-S. Li, Y. Sun, M.-M. Zhang, Y. Jiang, Optimized valence state of Co and Ni in high-entropy alloy for high active-stable OER, Rare Met. 42 (2023) 3607–3613.

[15] Q. Kang, M. Su, Y. Luo, T. Wang, F. Gao, Q. Lu, Chemical fermentation porecreation on multilevel bio-carbon structure with in situ Ni–Fe alloy loading for superior oxygen evolution reaction electrocatalysis, Nano-Micro Lett. 17 (2025) 269.

[16] X. Wang, J. Song, J. Ma, H. Du, J.J. Wang, L. Liu, H. Hu, W. Chen, Y. Zhou, J. Wang, M. Yang, L. Zhang, Surface-bound formate oxyanions destabilize hydration layers to pave OH^- transport pathways for oxygen evolution, ACS Catal. 14 (2024) 10871–10881.

[17] P. Liu, B. Chen, C. Liang, W. Yao, Y. Cui, S. Hu, P. Zou, H. Zhang, H.J. Fan, C. Yang, Tip-enhanced electric field: a new mechanism promoting mass transfer in oxygen evolution reactions, Adv. Mater. 33 (2021) 202007377.

[18] Z. Chen, M. Yang, Y. Li, W. Gong, J. Wang, T. Liu, C. Zhang, S. Hou, G. Yang, H. Li, Y. Jin, C. Zhang, Z. Tian, F. Meng, Y. Cui, Termination-aidity tailoring of molybdenum carbides for alkaline hydrogen evolution reaction, Nat. Commun. 16 (2025) 418.

[19] X. Ding, R. Jiang, J. Wu, M. Xing, Z. Qiao, X. Zeng, S. Wang, D. Cao, Ni_3N-CeO_2 heterojunction bifunctional catalysts for electrochemical water splitting, Adv. Funct. Mater. 33 (2023) 2306786.

[20] Z. Niu, Z. LU, Z. Qiao, S. Wang, X. Cao, X. Chen, J. Yun, L. Zheng, D. Cao, Robust Ru-VO_2 bifunctional catalysts for all-ph overall water splitting, Adv. Mater. 36 (2024) 2310690.

[21] M.F. Lagadec, A. Grimaud, Water electrolysers with closed and open electrochemical systems, Nat. Mater. 19 (2020) 1140–1150.

[22] Y. Zhou, Z. Wang, M. Cui, H. Wu, Y. Liu, Q. Ou, X. Tian, S. Zhang, NiFe-based electrocatalysts for alkaline oxygen evolution: challenges, strategies, and advances toward industrial-scale deployment, Adv. Fun. Mater. 34 (2024) 2410618.

[23] P. Zhou, X. Lv, S. Tao, J. Wu, H. Wang, X. Wei, T. Wang, B. Zhou, Y. Lu, T. Frauenheim, X. Fu, S. Wang, Y. Zou, Heterogeneous-interface-enhanced adsorption of organic and hydroxyl for biomass electrooxidation, Adv. Mater. 34 (2022) 2204089.

[24] J. Wu, Y. Chen, W. Du, Y. Hao, S. Wang, R. Wang, S. Cha, X. Yang, C. Yan, C. Lian, H. Liu, M. Gong, Concentrated zwitterion interfaces for selective promotion of electrochemical hydroxide oxidation, J. Am. Chem. Soc. 147 (2025) 32717.

[25] Y. Lin, B. Chen, D. Huang, Z. Yang, A. Lu, Z. Shi, Y. Liu, J. Fang, H. Li, T. Zhai, Solid-liquid interfacial hydrogen bond-mediated mass transfer toward industrial water electrolysis, Angew. Chem. Int. Ed. 64 (2025) e202502151.

[26] Y. Yan, M. Wu, L. Zhou, W. Chen, L. Han, G. Gao, Y. Cui, Z. Sun, A. Cabot, Enhancing electrocatalytic activity through targeted local electrolyte micro-environment, Adv. Funct. Mater. 35 (2025) 2419328.

[27] R. Fan, S. Lu, F. Wang, Y. Zhang, M. Hojamberdiev, Y. Chai, B. Dong, B. Zhang, Enhancing catalytic durability in alkaline oxygen evolution reaction through squaric acid anion intercalation, Nat. Commun. 16 (2025) 3407.

[28] J. Zhang, T. Quast, W. He, S. Dieckhöfer, J.R.C. Junqueira, D. Öhl, P. Wilde, D. Jambrec, Y.T. Chen, W. Schuhmann, Situ carbon corrosion and Cu leaching as a strategy for boosting oxygen evolution reaction in multimetal electrocatalysts, Adv. Mater. 34 (2022) 2109108.

[29] J. Guo, Y. Zheng, Z. Hu, C. Zheng, J. Mao, K. Du, M. Jaroniec, S.Z. Qiao, T. Ling, Direct seawater electrolysis by adjusting the local reaction environment of a catalyst, Nat. Energy 8 (2023) 264–272.

[30] S. Zhao, Y. Wang, Y. Hao, L. Yin, C.H. Kuo, H.Y. Chen, L. Li, S. Peng, Lewis acid driving asymmetric interfacial electron distribution to stabilize active species for efficient neutral water oxidation, Adv. Mater. 36 (2023) 2308925.

[31] H. Li, Y. Han, H. Zhao, W. Qi, D. Zhang, Y. Yu, W. Cai, S. Li, J. Lai, B. Huang, L. Wang, Fast site-to-site electron transfer of high-entropy alloy nanocatalysts driving redox electrocatalysis, Nat. Commun. 11 (2020) 5437.

[32] B. Ren, J. Huang, Q. Yuan, X. Liu, P. Li, G. Zhu, W. Xu, B. Dong, Tungsten defect-induced surface reconstruction of $Ce_2W_2O_9$ arrays for enhanced oxygen evolution reaction performance, Adv. Fun. Mater. 35 (2025) 2501328.

[33] H. Sun, X. Xu, Y. Song, W. Zhou, Z. Shao, Designing high-valence metal sites for electrochemical water splitting, Adv. Fun. Mater. 31 (2021) 2009779.

[34] R. Zhao, C. Zhang, L. Wei, D. Wei, J. Su, L. Guo, Tailoring a local acidic microenvironment on amorphous NiMoB catalyst to boost alkaline and neutral hydrogen evolution reactions, Appl. Catal. B Environ. Energy 365 (2025) 124928.

[35] Q. Sun, Y. Wang, Q. Cao, H. Hu, M. Zheng, Y. Xiao, Y. Liu, Y. Liang, A review of self-healing polymers for lithium batteries: from mechanistic insight to application, Sci. Energy Environ. 1 (2024) 6.

[36] L. Jia, F. Li, Carbon dioxide and nitrate electrocatalytic C-N coupling for sustainable production of urea, Sci. Energy Environ. 1 (2024) 2.

[37] S. Chen, G. Yang, Y. Jia, H. Zheng, Three-dimensional $NiCo_2O_4$@$NiWO_4$ core-shell nanowire arrays for high performance supercapacitors, J. Mater. Chem. A 5 (2017) 1028–1034.

[38] Z. Zhang, X. Li, C. Zhong, N. Zhao, Y. Deng, X. Han, W. Hu, Spontaneous synthesis of silver-nanoparticle-decorated transition-metal hydroxides for enhanced oxygen evolution reaction, Angew. Chem. Int. Ed. 59 (2020) 7245–7250.

[39] H. Ma, Y. Chen, H. Jin, X. Wang, G. Wang, Y. Fu, P. Wang, V. Subramaniam, K. Ramachandran, X. Liu, Constructing string-cage structure of α-MnO_2@CoS_2 photoelectrocatalyst for efficient detoxification sulfonamides wastewater, Sci. Energy Environ. 2 (2025) 6.

[40] Y. Li, Y. Wu, M. Yuan, H. Hao, Z. Lv, L. Xu, B. Wei, Operando spectroscopies unveil interfacial FeOOH induced highly reactive β-Ni(Fe)OOH for efficient oxygen evolution, Appl. Catal. B Environ. Energy 318 (2022) 121825.

[41] H. Li, S. Chen, Y. Zhang, Q. Zhang, X. Jia, Q. Zhang, L. Gu, X. Sun, L. Song, X. Wang, Systematic design of superaerophobic nanotube-array electrode comprised of transition-metal sulfides for overall water splitting, Nat. Commun. 9 (2018) 2452.

[42] N. Jian, H. Ge, Y. Ma, Y. Zhang, L. Li, J. Liu, J. Yu, C. Li, J. Li, Improved methanol-to-formate electrocatalytic reaction by engineering of nickel hydroxide and iron oxyhydroxide heterostructures, Sci. Energy Environ. 2 (2025) 3.

[43] J. Chen, C. Chen, M. Qin, B. Li, B. Lin, Q. Mao, H. Yang, B. Liu, Y. Wang, Reversible hydrogen spillover in Ru-WO_{3-x} enhances hydrogen evolution activity in neutral ph water splitting, Nat. Commun. 13 (2022) 5382.

[44] S.F. Zai, X.Y. Gao, C.C. Yang, Q. Jiang, Ce-modified $Ni(OH)_2$ nanoflowers supported on $NiSe_2$ octahedra nanoparticles as high-efficient oxygen evolution electrocatalyst, Adv. Energy Mater. 11 (2021) 2101266.

[45] J. Han, M.-M. Bai, T.-T. Ai, W.-W. Bao, X.-L. Wei, X.-Y. Zou, Z.-F. Deng, Y. Wang, W.-H. Li, J.-G. Hou, L.-J. Kou, Interface engineering and anion etching facilitating electronic modulation and surface reconstruction of FeSe@NiSe heterostructure catalysts to promote water splitting, Rare Met. 44 (2025) 1096–1107.

[46] J. Jiang, G. Xu, B. Gong, J. Zhu, W. Wang, T. Zhao, Y. Feng, Q. Wu, S. Liu, L. Zhang, Hydrogen spillover mechanism of superaerophobic $NiSe_2$-Ni_5P_4 electrocatalyst to promote hydrogen evolution in saline water, Adv. Funct. Mater. 35 (2024) 2412685.

[47] L. Deng, H. Chen, S.-F. Hung, Y. Zhang, H. Yu, H.-Y. Chen, L. Li, S. Peng, Lewis acid-mediated interfacial water supply for sustainable proton exchange membrane water electrolysis, J. Am. Chem. Soc. 146 (2024) 35438–35448.

[48] J. Huang, H. Sheng, R.D. Ross, J. Han, X. Wang, B. Song, S. Jin, Modifying redox properties and local bonding of Co_3O_4 by CeO_2 enhances oxygen evolution catalysis in acid, Nat. Commun. 12 (2021) 3036.
[49] Y. Song, M. Sun, S. Zhang, X. Zhang, P. Yi, J. Liu, B. Huang, M. Huang, L. Zhang, Alleviating the work function of vein-like Co_XP by Cr doping for enhanced seawater electrolysis, Adv. Fun. Mater. 33 (2023) 2214081.
[50] R. Qin, Q. Yao, W. Zeng, Z. Huang, H. Zhao, N. Chen, X. Huang, Facile reconstruction of Se-regulated NiMo nanorods for efficient anion exchange membrane water electrolysis, Nano Lett. 25 (2025) 4979–4986.
[51] H. Liu, Y. Shao, S. Dou, C. Pan, Enhanced photo-fenton degradation of antibiotics through internal electric field formation at the interface of mixed-phase FeS_2, Sci. Energy Environ. 1 (2024) 9.
[52] Y. Shi, W. Du, W. Zhou, C. Wang, S. Lu, S. Lu, B. Zhang, Unveiling the promotion of surface-adsorbed chalcogenate on the electrocatalytic oxygen evolution reaction, Angew. Chem. Int. Ed. 59 (2020) 22470–22474.
[53] M.I. Abdullah, Y. Fang, X. Wu, M. Hu, J. Shao, Y. Tao, H. Wang, Tackling activity-stability paradox of reconstructed $NiIrO_x$ electrocatalysts by bridged W-O moiety, Nat. Commun. 15 (2024) 10587.
[54] X. Ding, R. Jiang, J. Wu, M. Xing, Z. Qiao, X. Zeng, S. Wang, D. Cao, Ni3N–CeO2 heterostructure bifunctional catalysts for electrochemical water splitting, Adv. Fun. Mater. 33 (2023) 2306786.
[55] Q. Peng, X. Shao, C. Hu, Z. Luo, T. Taylor Isimjan, Z. Dou, R. Hou, X. Yang, Co_4S_3 grafted 1 *T*-phase dominated WS_2 ultrathin nanosheet arrays for highly efficient overall water splitting in alkaline media, J. Colloid Interface Sci. 615 (2022) 577.
[56] L. An, S. Zi, J. Zhu, Y. Zhai, Y. Hu, N. Zhang, S. Li, L. Liu, P. Xi, C.-H. Yan, Surface cladding engineering via oxygen sulfur distribution for stable electrocatalytic oxygen evolution reaction, Angew. Chem. Int. Ed. 64 (2024) e202413348.
[57] Y. Yang, Y. Kang, H. Zhao, X. Dai, M. Cui, X. Luan, X. Zhang, F. Nie, Z. Ren, W. Song, An interfacial electron transfer on tetrahedral NiS_2/$NiSe_2$ heterocages with dual-phase synergy for efficiently triggering the oxygen evolution reaction, Small 16 (2019) 1905083.
[58] M. Chen, Y. Zhang, R. Wang, B. Zhang, B. Song, Y. Guan, S. Li, P. Xu, Surface reconstruction of Se-doped NiS_2 enables high-efficiency oxygen evolution reaction, J. Energy Chem. 84 (2023) 173–180.
[59] S. Zhao, F. Hu, L. Yin, L. Li, S. Peng, Manipulating electron redistribution induced by asymmetric coordination for electrocatalytic water oxidation at a high current density, Sci. Bull. 68 (2023) 1389–1398.
[60] Z.-H. Yin, Y. Huang, K. Song, T.-T. Li, J.-Y. Cui, C. Meng, H. Zhang, J.-J. Wang, Ir single atoms boost metal-oxygen covalency on selenide-derived NiOOH for direct intramolecular oxygen coupling, J. Am. Chem. Soc. 146 (2024) 6846.
[61] S. Yang, X. Liu, X. Wang, Y. Lin, S. Cheng, H. Gao, F. Zhang, L. Li, J. Lian, U. Lassi, R. Ma, High-entropy type Fe-Ni-P-O-C amorphous nanospheres: remarkable Fe-ion migration induced efficient surface reconstruction for oxygen evolution reaction, Adv. Powder Mater. 4 (2025) 100329.
[62] F. Wu, F. Tian, M. Li, S. Geng, L. Qiu, L. He, L. Li, Z. Chen, Y. Yu, W. Yang, Y. Hou, Engineering lattice oxygen regeneration of NiFe layered double hydroxide enhances oxygen evolution catalysis durability, Angew. Chem. Int. Ed. 64 (2024) e202413250.
[63] X. Chen, X. Xu, Y. Cheng, H. Liu, D. Li, Y. Da, Y. Li, D. Liu, W. Chen, Achieving high-performance electrocatalytic water oxidation On $Ni(OH)_2$ with optimized intermediate binding energy enabled by S-doping and CeO_2-interfacing, Small 20 (2023) 2303169.
[64] C. Hu, K. Yue, J. Han, X. Liu, L. Liu, Q. Liu, Q. Kong, C.-W. Pao, Z. Hu, K. Suenaga, D. Su, Q. Zhang, X. Wang, Y. Tan, X. Huang, Misoriented high-entropy iridium ruthenium oxide for acidic water splitting, Sci. Adv. 9 (2023) eadf9144.
[65] X. Zhang, X. Wang, Q. Yan, R. Gao, J. Zhao, Z. Song, K. Zhu, D. Cao, J. Yao, L. Zheng, G. Wang, Defects engineering and interface regulation on Nickel-Rich sulphides promoting water/urea/ethanol eectrooxidation, Chem. Eng. J. 486 (2024) 150397.
[66] L. Zhou, Y. Shao, F. Yin, J. Li, F. Kang, R. Lv, Stabilizing non-iridium active sites by non-stoichiometric oxide for acidic water oxidation at high current density, Nat. Commun. 14 (2023) 7644.
[67] X. Zhang, X. Liu, D. Wu, L. Hu, H. Zhang, Z. Sun, S. Qian, Z. Xia, Q. Luo, L. Cao, J. Yang, T. Yao, Self-assembly intermetallic $PtCu_3$ core with high-index faceted Pt shell for high-efficiency oxygen reduction, Nano Lett. 24 (2024) 3213–3220.
[68] Z. Xie, H. Chen, X. Wang, Y.A. Wu, Z. Wang, S. Jana, Y. Zou, X. Liang, X. Zhao, X. Zou, Honeycomb-structured IrO_x foam platelets as the building block of anode catalyst layer in PEM water electrolyzer, Angew. Chem. Int. Ed. 64 (2024) e202415032.
[69] Z. Liang, D. Shen, Y. Wei, F. Sun, Y. Xie, L. Wang, H. Fu, Modulating the electronic structure of cobalt-vanadium bimetal catalysts for high-stable anion exchange membrane water electrolyzer, Adv. Mater. 36 (2024) 2408634.
[70] X. Zhong, J. Xu, J. Chen, X. Wang, Q. Zhu, H. Zeng, Y. Zhang, Y. Pu, X. Hou, X. Wu, Y. Niu, W. Zhang, Y.A. Wu, Y. Wang, B. Zhang, K. Huang, S. Feng, Spatially and temporally resolved dynamic response of co-based composite interface during the oxygen evolution reaction, J. Am. Chem. Soc. 146 (2024) 7467–7479.
[71] Q. Wang, Y. Gong, X. Zi, L. Gan, E. Pensa, Y. Liu, Y. Xiao, H. Li, K. Liu, J. Fu, J. Liu, A. Stefancu, C. Cai, S. Chen, S. Zhang, Y.R. Lu, T.S. Chan, C. Ma, X. Cao, E. Cortés, M. Liu, Coupling nano and atomic electric field confinement for robust alkaline oxygen evolution, Angew. Chem. Int. Ed. 63 (2024) e202405438.
[72] J. Liang, Z. Li, M. Zhang, H. Wang, Z. Cai, Y. Luo, F. Luo, T. Wu, Y. Yao, B. Tang, X. Sun, Amorphous phosphates tailor local proton supply for alkaline hydrogen evolution electrocatalysis, Adv. Mater. 37 (2025) 202503660.
[73] Y. Feng, W. Zhu, J. Xu, D. Zhang, Q. Ma, L. Zhao, L. Lin, Q. Su, Y. Wang, Q. Liu, Y. Wei, X. Li, J. Huang, Y. Ye, J. Zhao, B. Wu, Steering the electronic microenvironment of ruthenium sites via boron buffering enables enhanced hydrogen evolution under a universal pH range, ACS Nano 19 (2025) 7948–7961.
[74] Z. Qiao, R. Jiang, J. Yun, D. Cao, Why the abnormal phenomena of D-band center theory exists? A new BASED theory for surface catalysis and chemistry, Chin. J. Catal. 64 (2024) 44–53.
[75] H. Xu, D. Cheng, D. Cao, X. Zeng, Revisiting the universal principle for a rational design of single - atom electrocatalysts, Nat. Catal. 7 (2024) 207–218.
[76] F. Wei, J. Shen, J. Xie, Z. Luo, L. Shi, T. Taylor Isimjan, X. Yang, J. Qiu, B. Wu, Dynamic in situ reconstruction of $NiSe_2$ promoted by interfacial $Ce_2(CO_3)_2O$ for enhanced water oxidation, J. Energy Chem. 98 (2024) 472.
[77] C. Liu, Y. Han, L. Yao, L. Liang, J. He, Q. Hao, J. Zhang, Y. Li, H. Liu, Engineering bimetallic NiFe-based hydroxides/selenides heterostructure nanosheet arrays for highly-efficient oxygen evolution reaction, Small 17 (2021) 2007334.
[78] Y. Bai, Y. Wu, X. Zhou, Y. Ye, K. Nie, J. Wang, M. Xie, Z. Zhang, Z. Liu, T. Cheng, C. Gao, Promoting Nickel oxidation state transitions in single-layer nifeb hydroxide nanosheets for efficient oxygen evolution, Nat. Commun. 13 (2022) 6094.
[79] S. Li, T. Liu, W. Zhang, M. Wang, H. Zhang, C. Qin, L. Zhang, Y. Chen, S. Jiang, D. Liu, X. Liu, H. Wang, Q. Luo, T. Ding, T. Yao, Highly efficient anion exchange Membrane Water Electrolyzers via Chromium-Doped Amorphous Electrocatalysts, Nat. Commun. 15 (2024) 3416.
[80] J. Wang, Y. Liu, G. Yang, Y. Jiao, Y. Dong, C. Tian, H. Yan, H. Fu, MXene-assisted NiFe sulfides for high-performance anion exchange membrane seawater electrolysis, Nat. Commun. 16 (2025) 1319.
[81] Z.-F. Huang, S. Xi, J. Song, S. Dou, X. Li, Y. Du, C. Diao, Z.J. Xu, X. Wang, Tuning of lattice oxygen reactivity and scaling relation to construct better oxygen evolution electrocatalyst, Nat. Commun. 12 (2021) 3992.